Inorganic Chemistry
Cite This: *Inorg. Chem.* XXXX, XXX, XXX−XXX
Article
pubs.acs.org/IC

Redox-Active Zeolitic Transition Metal Oxides Based on ε-Keggin Units for Selective Oxidation

Zhenxin Zhang,*[,†] Satoshi Ishikawa,[‡] Qianqian Zhu,[†] Toru Murayama,[§] Masahiro Sadakane,[∥] Michikazu Hara,[⊥] and Wataru Ueda*[,‡]

[†]School of Material Science and Chemical Engineering, Ningbo University, Fenghua Road 818, Ningbo, Zhejiang 315211, P. R. China
[‡]Faculty of Engineering, Kanagawa University, Rokkakubashi, Kanagawa-ku, Yokohama-shi, Kanagawa 221-8686, Japan
[§]Research Center for Gold Chemistry, Graduate School of Urban Environmental Sciences, Tokyo Metropolitan University, 1-1 Minami-Osawa, Hachioji, Tokyo 192-0397, Japan
[∥]Department of Applied Chemistry, Hiroshima University, 1-4-1 Kagamiyama, Higashi Hiroshima 739-8527, Japan
[⊥]Materials and Structures Laboratory, Tokyo Institute of Technology, Nagatsuta-cho 4259, Midori-ku, Yokohama-city, Kanagawa 226-8503, Japan

Supporting Information

ABSTRACT: The design and development of zeolitic transition metal oxides for selective oxidation are interesting due to the combination of the redox properties and microporosities. Redox-active zeolitic transition metal oxides based on ε-Keggin iron molybdates were synthesized. O_2 can be activated by the materials via an electron-transfer-based process, and the materials can be oxidized even at room temperature. The materials are oxidized and reduced reversibly while the crystal structures are maintained. V is uniformly incorporated in the materials without changing the basic structures, and the redox properties of the materials are tuned by V. The materials are used as robust catalysts for ethyl lactate oxidation to form ethyl pyruvate using O_2 as an oxidant.

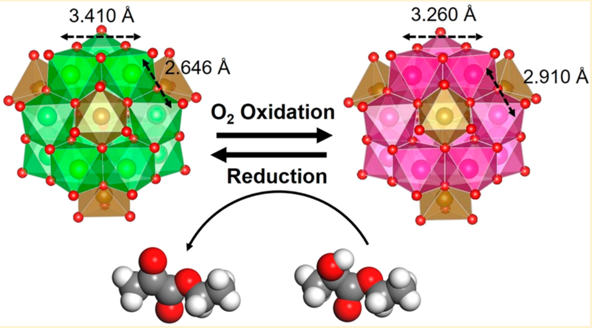

INTRODUCTION

Inorganic crystalline microporous materials, such as zeolites, have attracted much attention as ideal catalytic materials from scientific and industrial communities due to the unique structural features, such as uniform channels and cavities, well-defined crystal structures, high surface area, and tunable structures and porosity.[1−3] In chemical composition, zeolites are mainly composed of main group elements, which are less attractive compared with transition metal oxides for particularly redox-based reactions because transition metal oxides exhibit a multielectron-transfer property.[4−6] Furthermore, transition metal oxides show elemental diversity and complexity, which enable the tuning of the redox properties accordingly.

Zeolitic transition metal oxides representing another of inorganic microporous material are recognized as ideal catalytic materials that combine the significant features of microporous materials and transition metal oxides. However, their design and synthesis are still challenging. To date, only a few examples of zeolitic transition metal oxides have been reported, such as cubane-unit-based [W_4O_{16}-based] vanadotungstates,[7] pentagon-unit-based vanadomolybdates,[8−10] ring-shaped polyoxometalate-based (POM-based) tungstates,[11,12] and ε-Keggin POM-based molybdates.[13,14]

Among these zeolitic transition metal oxides, the materials based on ε-Keggin POM are interesting and are constructed by the assembly of ε-Keggin POM, [$Mo_{12}O_{40}$], and metal ions as linkers. The cavity of the materials is surrounded by 10 POM units and linkers and is opened after removal of the original guest molecules. The materials show high elemental diversity, and the chemical compositions of the materials are able to be modified by tuning the Keggin unit, the linker, and the countercations, which affects the properties and applications of the materials.[15] The Mo ions in the materials are oxidized with the structures maintained, indicating that the materials would have a redox property.[14,16]

O_2 activation is a crucial topic for selective oxidation. O_2 activation via a radical process is less useful in this field because the radical leads to autoxidation. O_2 activation via an electron-transfer-based redox process is more important and generally includes two steps: (1) substrate oxidation by catalysts and (2) catalysts reoxidation with O_2. Transition metals are able to store and transfer electrons,[17] and the multicomponent would enhance the ability.[18,19] Therefore, design and synthesis of

Received: February 20, 2019

redox-active zeolitic transition metal oxides are desired for catalytic oxidation.

Herein, we reported the synthesis, structural characterization, redox property, and catalytic application of zeolitic transition metal oxides based on iron molybdates (**$MoFe_{0.22}O$**). Structural analysis with powder X-ray diffraction and elemental analysis demonstrated that the materials were based on ε-Keggin POM units with Fe as linkers and cations. V was able to be incorporated into the materials with the crystal structure maintained, and the resulting materials were denoted as **$MoFe_{0.17}V_{0.07}O$**, **$MoFe_{0.14}V_{0.12}O$**, and **$MoFe_{0.11}V_{0.18}O$**, separately. Electron transfer from O_2 to the materials occurred even at room temperature, leading to a unique O_2 adsorption behavior and oxidation of the materials. The oxidized materials were reduced reversibly with the crystal structure maintained. Due to the redox property, the materials catalyzed the selective oxidation of ethyl lactate (EL) to form ethyl pyruvate (EP) using O_2 as an oxidant.

■ EXPERIMENTAL SECTION

Material Preparation. *Synthesis of $MoFe_{0.22}O$ and $MoFeV_xO$.* The total molar content of Mo and V was 11.7 mmol. Ammonium heptamolybdate (AHM) $(NH_4)_6Mo_7O_{24}\cdot4H_2O$ ($11.7 - x$ mmol based on Mo) and NH_4VO_3 (x mmol based on V), where x = 0, 0.585, 1.17, and 2.34 mmol, were dissolved in 40 mL of distilled water. Metal Mo (0.2 g, 2.1 mmol) and Fe_3O_4 (0.258 g, 1.1 mmol) were added to the mixture sequentially. The mixture was introduced into a 50 mL stainless-steel autoclave with a Teflon liner. The autoclave was fixed in an oven with a mechanical rotation system. Hydrothermal synthesis was performed at 175 °C with tumbling (1−2 rpm) for 48 h. After the autoclave had been cooled down, the crude solid was moved to a 100 mL beaker, and 60 mL of water was added. The unreacted Fe_3O_4 was completely removed by a magnet. The resulting suspension was centrifuged (3500 rpm, 30 min), and solids on the bottom of the centrifugation tube were collected. The collected solid was washed with water by dispersing in 10 mL of water and subsequent centrifugation (3500 rpm, 30 min). After the washing process was repeated two more times, the obtained solid was dried. The resulting 1.185, 1.203, 0.923, and 0.852 g of **$MoFe_{0.22}O$**, **$MoFe_{0.17}V_{0.07}O$**, **$MoFe_{0.14}V_{0.12}O$**, and **$MoFe_{0.11}V_{0.18}O$** were obtained with the yields of 59%, 60%, and 45%, and 40% based on Mo, respectively.

Elemental Analysis. Anal. Calcd for **$MoFe_{0.22}O$** ($N_2Fe_{2.6}Mo_{12}O_{43}H_{22.1}$): Fe, 7.08; Mo, 55.98; N, 1.36; H, 1.35. Found: Fe, 7.14; Mo, 56.46; N, 1.29; H, 1.00.

Anal. Calcd for **$MoFe_{0.17}V_{0.07}O$** ($N_2Fe_{2.0}Mo_{11.8}V_{0.8}O_{43}H_{23.5}$): Fe, 5.53; Mo, 55.92; V, 2.01; N, 1.38; H, 1.16. Found: Fe, 5.58; Mo, 56.00; V, 2.18; N, 1.37; H, 1.24.

Anal. Calcd for **$MoFe_{0.14}V_{0.12}O$** ($N_2Fe_{1.6}Mo_{11.6}V_{1.4}O_{43}H_{21.1}$): Fe, 4.46; Mo, 55.34; V, 3.55; N, 1.39; H, 1.05. Found: Fe, 4.37; Mo, 55.60; V, 3.57; N, 1.54; H, 1.25.

Anal. Calcd for **$MoFe_{0.11}V_{0.18}O$** ($N_2Fe_{1.2}Mo_{11.4}V_{2.0}O_{48}H_{27}$): Fe, 3.22; Mo, 52.44; V, 4.88; N, 1.34; H, 1.29. Found: Fe, 3.30; Mo, 51.94; V, 4.93; N, 1.26; H, 1.63.

Synthesis of Other ε-Keggin-Based Materials. The materials of **MoZnO**,[14] **MoMnO**,[14] **MoCoO**,[20] and **MoVBiO**[13] were synthesized according to the literature. Briefly, sodium molybdate or AHM was mixed with a reducing agent, followed by the addition of linker sources, such as $ZnCl_2$, MnO, Co_3O_4, and $Bi(OH)_3$. The mixture was set in an oven for hydrothermal synthesis for 1−2 days at 175 °C with tumbling (1−2 rpm). After purification, the materials were recovered as catalysts.

Ion-Exchange Process. **$MoFe_{0.22}O$** (0.3 g) was dispersed in 15 mL of water. CsCl (1.027 g, 6.11 mmol) was added to the solution. The mixture was stirred at room temperature for 24 h under Ar protection. The resulting material was isolated from the solution by centrifugation and washed with water 3 times. Anal. Calcd for **$CsMoFe_{0.22}O$** ($Cs_{0.4}N_2Fe_{2.4}Mo_{12}O_{48}H_{27.7}$): Fe, 6.17; Mo, 52.87. Found: Fe, 6.23; Mo, 52.75. **MoZnO** (0.3 g) was dispersed in 15 mL of water; $FeSO_4\cdot7H_2O$ (0.339 g, 1.22 mmol) was added in the solution. The mixture was stirred at room temperature under Ar protection for 24 h. The resulting material was isolated from the solution by centrifugation and washed with water 3 times. Anal. Calcd for **FeMoZnO** ($Fe_{0.6}Na_{0.5}Zn_3Mo_{12}O_{49}H_{29.2}$): Fe, 1.52; Na, 0.52; Mo, 52.22; Zn, 8.85. Found: Fe, 1.59; Na, 0.58; Mo, 51.88; Zn, 9.21.

Characterization. Powder X-ray diffraction (XRD) patterns were obtained on a RINT2200 (Rigaku) instrument with Cu Kα radiation (tube voltage, 40 kV; tube current, 20 mA). Fourier transform infrared (FTIR) analysis was carried out on JASCO-FTIR-6100 (JASCO). X-ray photoelectron spectroscopy (XPS) was performed on a JPS-9010MC (JEOL) instrument. The spectrometer energies were calibrated using the C 1s peak at 284.7 eV. The scanning electron microscopy (SEM) image was obtained with an SU-8010 system (HITACHI). The transmission electron microscopy (TEM) image was taken with a 200 kV TEM (JEOL JEM-2100F) instrument. Elemental composition was determined by an inductive coupling plasma (ICP-AES) method (ICPE-9000, Shimadzu). CHN elemental compositions were determined at the Material Analysis Suzukake-dai Center, Technical Department, Tokyo Institute of Technology. Temperature-programmed desorption−mass spectrometry (TPD−MS) measurements were carried out from 40 to 620 °C at a heating rate of 10 °C/min under He flow (flow rate: 50 mL/min). Samples were set up between two layers of quartz wool. A TPD apparatus (BEL Japan, Inc.) equipped with a quadrupole mass spectrometer (M-100QA. Anelva) was used to detect NH_3 (m/z = 16) and H_2O (m/z = 18). Temperature-programmed oxidation−mass spectrometry (TPO−MS) measurements were carried out on a BELCAT II (BEL Japan Inc.) instrument from 40 to 700 °C at a heating rate of 10 °C/min under He-diluted O_2 (3%) with a total flow rate of 50 mL/min. O_2 (m/z = 32) was monitored by a quadrupole mass spectrometer. Gas adsorption−desorption measurements were performed on **$MoFe_{0.22}O$** and **$MoFeV_xO$** by a BELSORP MAX (BEL Japan Inc.) sorption analyzer. The samples were evacuated at 200 °C for 2 h before the measurement. N_2 adsorption−desorption measurements were carried out at −196 °C, and O_2 adsorption−desorption measurements were carried out at 25 °C.

Structure Analysis. The structures of **$MoFe_{0.22}O$** and **$MoFeV_xO$** were determined by powder XRD. The high-quality powder XRD pattern was recorded on an RINT2200 (Rigaku) instrument with Cu Kα radiation (tube voltage, 40 kV; tube current, 40 mA; scan speed, 1°/min; step, 0.01°). First, the powder XRD pattern was indexed by DICVOL06[21] and X-cell[22] programs. After Pawley refinement was performed, the most reasonable space group was obtained. Then, the Le Bail method was applied for intensity extraction with the EdPCR program. The initial structure was solved by a charge-flipping algorithm.[23] The positions and types of heavy metal atoms (Mo and Fe) were obtained by analyzing the generated electron density maps. Most of the oxygen atoms and cations were assigned according to the residual peaks, which were indicated by the charge-flipping algorithm. The initial structures from the charge-flipping algorithm are shown in Table S1.

The initial structure of **$MoFe_{0.22}O$** was refined by powder XRD Rietveld refinement using the Materials Studio package (Accelrys Software Inc.).[24] The lattice parameters and pattern parameters of the material were first refined by Pawley refinement. Then, isotropic temperature factors were given for every atom in the initial structure. Rietveld analysis was started with the initial model of the material and lattice parameters and pattern parameters from Pawley refinement. Every atom position was refined. The occupancy of atoms in the framework was fixed without further refinement, and occupancies of atoms in micropores were refined with consideration of the elemental analysis results. Finally, the pattern parameters were refined again to obtain the lowest R_{wp} value. Crystallographic parameters and Rietveld analysis parameters are shown in Table S2. Atom position, temperature factor, occupancy, and bond length are shown in Tables S3−S8.

DOI: 10.1021/acs.inorgchem.9b00502

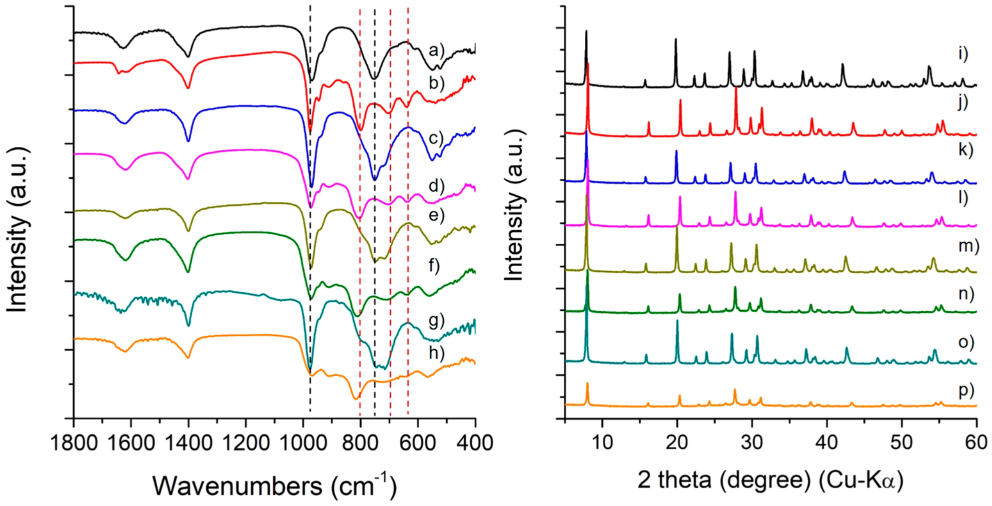

Figure 1. FTIR spectra of (a) $\mathbf{MoFe_{0.22}O}$, (b) $\mathbf{MoFe_{0.22}OAC150}$, (c) $\mathbf{MoFe_{0.17}V_{0.07}O}$, (d) $\mathbf{MoFe_{0.17}V_{0.07}OAC150}$, (e) $\mathbf{MoFe_{0.14}V_{0.12}O}$, (f) $\mathbf{MoFe_{0.14}V_{0.12}OAC150}$, (g) $\mathbf{MoFe_{0.11}V_{0.18}O}$, and (h) $\mathbf{MoFe_{0.11}V_{0.18}OAC150}$. XRD patterns of (i) $\mathbf{MoFe_{0.22}O}$, (j) $\mathbf{MoFe_{0.22}OAC150}$, (k) $\mathbf{MoFe_{0.17}V_{0.07}O}$, (l) $\mathbf{MoFe_{0.17}V_{0.07}OAC150}$, (m) $\mathbf{MoFe_{0.14}V_{0.12}O}$, (n) $\mathbf{MoFe_{0.14}V_{0.12}OAC150}$, (o) $\mathbf{MoFe_{0.11}V_{0.18}O}$, and (p) $\mathbf{MoFe_{0.11}V_{0.18}OAC150}$.

Calcination Experiment. For air calcination, 0.3 g of the materials was introduced in a ceramic crucible, which was heated in a muffle furnace. The temperature was increased to the desired temperature with a ramp of 10 °C/min under a static air atmosphere; then, the temperature was maintained for 2 h. For H_2 treatment, 0.3 g of the materials was introduced into the glass tubular reactor, which was heated at the desired temperature with a ramp of 10 °C/min and H_2 flow rate of 10 mL/min. The temperature was maintained for 2 h.

Catalytic Oxidation of Ethyl Lactate. The catalytic oxidation of EL to EP was carried out using a fixed bed stainless tubular reactor at atmospheric pressure. For a typical reaction, the powder catalyst (0.5 g) was introduced into the glass tubular reactor. The reactor was heated to 200 °C with an increasing rate of 10 °C/min under air flow (N_2 15.6 mL/min, O_2 4.2 mL/min). The temperature was measured with a thermal-couple inserted in the catalyst zone. When the temperature reached 200 °C, EL was introduced in the system by a pump with a flow rate of 1.95 mL/min. The reactant and products were trapped and collected every hour at 0 °C in the outlet of the reactor after the reaction was stabilized for 20 min. After decane was added as an internal standard to the trap, the reactant and products were analyzed with a gas chromatograph with an FID detector. Selectivity to EP (%) = (produced EP (mmol)/converted EL (mmol)) × 100%. EP yield (%) = (produced EP (mmol)/total EL (mmol)) × 100%.

■ RESULTS AND DISCUSSION

Material Synthesis. Zeolitic transition metal oxides based on ε-Keggin POM were expected to contain different kinds of transition metal elements. Several isostructural materials were able to be synthesized.[13,14] $\mathbf{MoFe_{0.22}O}$ was synthesized by a hydrothermal method, using the starting materials of AHM as a molybdenum source, Mo as a reducing agent, and Fe_3O_4 as a linker ion. The crude solid obtained after hydrothermal synthesis was purified to remove the unreacted Fe_3O_4 and Mo. $\mathbf{MoFe_{0.22}O}$ was not obtained without reducing agent (metallic Mo; Figure S1). V was incorporated in $\mathbf{MoFe_{0.22}O}$ by adding NH_4VO_3 in the precursor solution. The different amounts of NH_4VO_3 were introduced in the precursor solutions to obtain the materials with different V contents.

Material Characterization. The FTIR spectrum of $\mathbf{MoFe_{0.22}O}$ (Figure 1a–h) was similar to those of other molecular ε-Keggin polyoxomolybdates[25] and ε-Keggin POM-based zeolitic transition metal oxides.[13,14,20,26] The peak at 1620 cm^{-1} was ascribed to water, and the peak at 1402 cm^{-1} was ascribed to NH_4^+. The peaks below 1000 cm^{-1} were derived from the ε-Keggin POM unit. The Mo═O terminal bond showed a signal at 974 cm^{-1}, and the Mo—O—Mo bridging bonds showed a peak at 753 cm^{-1}. After incorporation of V in $\mathbf{MoFe_{0.22}O}$, there were new IR bands generated around 750 cm^{-1}, which demonstrated that $\mathbf{MoFe_{0.22}O}$ successfully incorporated V in the structure. V in the materials might change the bonding state of the molecule, causing the FTIR band change.

SEM images showed an octahedral-shaped particle for $\mathbf{MoFe_{0.22}O}$, $\mathbf{MoFe_{0.17}V_{0.07}O}$, $\mathbf{MoFe_{0.14}V_{0.12}O}$, and $\mathbf{MoFe_{0.11}V_{0.18}O}$ (Figure S2), and the particle sizes of the materials were smaller than 100 nm in diameter. Energy-dispersive X-ray (EDX) analysis indicated that the materials incorporated Mo, V, and Fe. Elemental mapping showed that Mo, V, and Fe uniformly distributed in the crystals, which demonstrated that V was incorporated in the structure of the materials.

Quantitatively, the V content in the materials was determined by elemental analysis, which revealed that the component of V increased with increasing the content of NH_4VO_3 in the precursor solution. The ratio of N/Mo/Fe/V was 2/12/2.6/0, 2/11.8/2.0/0.8, 2/11.6/1.6/1.4, and 2/11.4/1.2/2.0, for $\mathbf{MoFe_{0.22}O}$, $\mathbf{MoFe_{0.17}V_{0.07}O}$, $\mathbf{MoFe_{0.14}V_{0.12}O}$, and $\mathbf{MoFe_{0.11}V_{0.18}O}$, respectively. The materials were also able to be synthesized with the molar ratio of AHM (based on Mo), NH_4VO_3, and Fe_3O_4 (based on Fe) the same as the molar ratio of Mo, V, and Fe in the materials (Figure S3). Elemental analysis indicated that V in the materials was able to be controlled by the NH_4VO_3 content of the precursor solution (Table 1). The Mo and Fe ratio decreased obviously after V incorporation, and therefore, V substituted both Mo and Fe in the material.

Powder XRD patterns of $\mathbf{MoFe_{0.22}O}$, $\mathbf{MoFe_{0.17}V_{0.07}O}$, $\mathbf{MoFe_{0.14}V_{0.12}O}$, and $\mathbf{MoFe_{0.11}V_{0.18}O}$ were similar to the reported zeolitic transition metal oxide based on ε-Keggin POM,[14] indicating that the basic structures of the materials were the same (Figure 1i,k,m,o). The diffraction peak shifted to a higher angle with the increase in the V content in the

DOI: 10.1021/acs.inorgchem.9b00502

Table 1. Chemical Composition of $MoFeV_xO$ Based on Elemental Analysis

material	POM unit	linker[a]	cation[a]	composition			oxidation states			chemical formula
				Mo	Fe	V	Mo	Fe	V	
$MoFe_{0.22}O$	$[Fe_{2.0}Mo_{12}O_{40}]$	Fe (2.0)	NH_4^+ (2), Fe^{2+} (0.6)	12	2.6	0	$Mo^{VI}/Mo^{V} = 0.10$	Fe^{II}		$(NH_4)_2Fe^{II}{}_{0.6}H_{11.7}[Fe^{II}{}_{2.0}Mo^{VI}{}_{1.1}Mo^{V}{}_{10.9}O_{40}]$
$MoFe_{0.17}V_{0.07}O$	$[Fe_{1.4}Mo_{11.8}V_{0.8}O_{40}]$	Fe (1.4), V (0.6)	NH_4^+ (2), Fe^{2+} (0.6)	11.8	2.0	0.8	$Mo^{VI}/Mo^{V} = 0.15$	Fe^{II}	V^{IV}	$(NH_4)_2Fe^{II}{}_{0.6}H_{10.3}[Fe^{II}{}_{1.4}Mo^{VI}{}_{1.5}Mo^{V}{}_{10.3}V^{IV}{}_{0.8}O_{40}]$
$MoFe_{0.14}V_{0.12}O$	$[Fe_{1.0}Mo_{11.6}V_{1.4}O_{40}]$	Fe (1.0), V (1.0)	NH_4^+ (2), Fe^{2+} (0.6)	11.6	1.6	1.4	$Mo^{VI}/Mo^{V} = 0.31$	Fe^{II}	V^{IV}	$(NH_4)_2Fe^{II}{}_{0.6}H_{8.5}[Fe^{II}{}_{1.0}Mo^{VI}{}_{2.7}Mo^{V}{}_{8.9}V^{IV}{}_{1.4}O_{40}]$
$MoFe_{0.11}V_{0.18}O$	$[Fe_{0.6}Mo_{11.4}V_{2.0}O_{40}]$	Fe (0.6), V (1.4)	NH_4^+ (2), Fe^{2+} (0.6)	11.4	1.2	2.0	$Mo^{VI}/Mo^{V} = 0.98$	Fe^{II}	V^{IV}	$(NH_4)_2Fe^{II}{}_{0.6}H_{5}[Fe^{II}{}_{0.6}Mo^{VI}{}_{5.6}Mo^{V}{}_{5.8}V^{IV}{}_{2.0}O_{40}]$

[a] The number in brackets means the number of the species per chemical formula.

materials, which indicated a decrease in lattice parameters, 19.5498, 19.4485, 19.3839, and 19.3216 Å for **$MoFe_{0.22}O$**, **$MoFe_{0.17}V_{0.07}O$**, **$MoFe_{0.14}V_{0.12}O$**, and **$MoFe_{0.11}V_{0.18}O$**, respectively.

The crystal structure of **$MoFe_{0.22}O$** was determined by the powder XRD with the charge-flipping algorithm (Figure 2a). There were three sites in the material, the surrounding site, central site, and linker site. The ratio of the surrounding site/central site/linker site was 12/1/2. The electron density map after the charge-flipping algorithm showed that the electron densities of the surrounding site and the linker site were most intensive (Figure 2b,c and Table S1), and the electron density of the surrounding site was heavier than that of the linker site. Therefore, we assumed that the surrounding site was occupied by Mo, and the linker site was occupied by Fe. There was no strong electron density being observed in the central site, indicating that the central site might not be occupied by the heavy elements (Mo and Fe). Therefore, the building block of the material was the ε-Keggin POM unit, $[\varepsilon\text{-}Mo_{12}O_{40}]$, which is formed by 12 MoO_6 octahedra in a T_d symmetry with an empty central site, which also existed in other ε-Keggin POM molecules.[25] The POM units were connected by Fe as linkers to form the microporous framework (Figure 2d,e). The simulated XRD pattern of the proposed structure was similar to the experimental data, concluding that the structure was correct (Figure S4a).

Furthermore, the ratio of Fe/Mo = 2.6/12 was not stoichiometric while the ratio of linker site/surrounding site was only 2/12. There was excessive Fe compared with the linker site, and therefore, the additional Fe might be located in other sites. Because no strong electron density was observed in the center of the Keggin unit, we assumed that the additional Fe mainly acted as cations. Cs^+ exchange was carried out for **$MoFe_{0.22}O$**. After ion-exchange, the structure of the material did not change, as the characteristic peaks of XRD patterns and FTIR spectra of the materials did not change (Figure S5). Elemental analysis demonstrated that Fe was partially exchanged by Cs^+ in the aqueous solution (see the Experimental Section for elemental analysis), which indicated that the additional Fe might be derived from the cation species.

In the case of **$MoFeV_xO$**, V substituted both Mo and Fe, and thus, it occupied not only the surrounding sites but also the linker site. V^V tended not to be a free cation of the material, and thus, we assumed that V mainly replaced the linker Fe.

Figure S6 shows a high-resolution TEM image of the material along the [1 0 1] direction. The lattice parameter of the unit cell and distance of the (1 1 1) plane were also obtained from the high-resolution TEM (HRTEM) image, which was in good agreement with the results obtained from the crystal structure of **$MoFe_{0.22}O$**.

Oxidation states of the metal elements were determined by XPS, and the profiles are presented in Figure 3. For **$MoFe_{0.22}O$**, the 12 Mo atoms were mostly reduced, and the ratio of Mo^{VI}/Mo^{V} was 0.1 (Figure 3a). The oxidation state of Mo increased gradually with increasing the V content in the materials. Mo^{VI}/Mo^{V} was 0.15, 0.31, and 0.98 for **$MoFe_{0.17}V_{0.07}O$**, **$MoFe_{0.14}V_{0.12}O$**, and **$MoFe_{0.11}V_{0.18}O$**, respectively (Figure 3c,e,g and Table 1). NH_4VO_3 might oxidize the reduced Mo ions. XPS profiles showed the V signal after incorporation of V in the material, and the oxidation state of V was V^{IV} (Figure 3i−n).[27−29] Fe in the materials was also detected and determined to be Fe^{II} (Figure 3o−v).[30−32] In addition, O XPS was obtained for each material, which showed

DOI: 10.1021/acs.inorgchem.9b00502
Inorg. Chem. XXXX, XXX, XXX−XXX

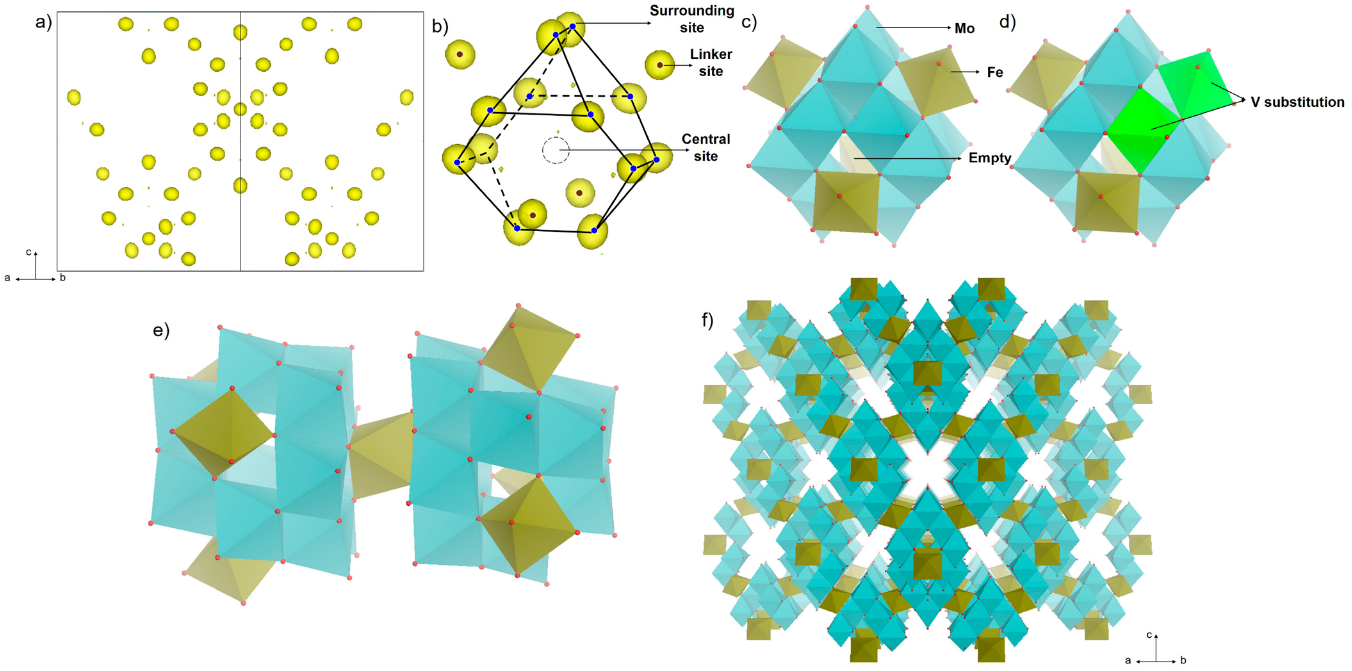

Figure 2. Electron density map of $\mathbf{MoFe_{0.22}O}$ obtained after the charge-flipping algorithm. (a) Unit cell and (b) Keggin unit. (c) Structure representations of the ε-Keggin POM units. (d) Structure representations of the ε-Keggin POM units with V sites. (e) Linkage of ε-Keggin POM units with Fe. (f) Framework of the material: Mo or V (blue), Fe in linker (orange), O (red).

the same peak position and was similar to the previous report (Figure S7).[33] The chemical formulas of the materials are estimated in Table 1.

The occupied guest molecules, such as water and NH_3, were monitored by TPD−MS. For $\mathbf{MoFe_{0.22}O}$, there was a desorption peak for m/z = 18, which was ascribed to water desorption (Figure S8). The desorption peak at a low temperature was ascribed to the weakly bound water. The rest of the peaks that appeared at higher temperatures were ascribed to water formed by deprotonation with lattice oxygen. The NH_4^+ showed desorption from $\mathbf{MoFe_{0.22}O}$ at 300−350 °C. After V substitution, the peak position of NH_4^+ shifted to a lower temperature, which indicated that V substitution decreased the interaction of NH_4^+ and the framework.

Microporosity of the materials before and after V incorporation was investigated by the N_2 adsorption−desorption measurements. The materials did not adsorb N_2 at −196 °C, although the materials were pretreated at 200 °C to remove water to open the micropore (Figure S9). The micropores of the materials might be too small to adsorb N_2. The surface areas of the materials based on the BET method were 20, 21, 24, and, 26 m^2/g for $\mathbf{MoFe_{0.22}O}$, $\mathbf{MoFe_{0.17}V_{0.07}O}$, $\mathbf{MoFe_{0.14}V_{0.12}O}$, and $\mathbf{MoFe_{0.11}V_{0.18}O}$, respectively, indicating that after incorporating V the particle size of the materials decreased slightly. Although the micropore could not adsorb N_2, it was enough for adsorbing a smaller molecule such as CO_2 (Figure S10).

Redox Property of $\mathbf{MoFe_{0.22}O}$. *Oxidation.* The investigations on the redox properties of the materials and the related electron-transfer process are important for O_2 activation and catalytic oxidation. Temperature-dependent investigations of the thermal stability of $\mathbf{MoFe_{0.22}O}$ and $\mathbf{MoFeV_{\mathit{x}}O}$ were conducted in air, and the resulting materials were denoted as $\mathbf{MoFe_{0.22}OAC150}$ and $\mathbf{MoFeV_{\mathit{x}}OAC150}$. The resulting materials were investigated by XRD (Figure S11). The structures of the materials were stable at 200 °C. The XRD patterns of the materials did not change, and the basic crystal structures of the materials were stable. When the treatment temperature was further increased, the intensity of the diffraction peaks of the material became weak and broadened, indicating that the materials started to decompose.

The valences of metal ions in the materials before and after calcination at 150 °C were confirmed by XPS (Figure 3b,d,f,h). After calcination in air, Mo^V was mainly oxidized to Mo^{VI} in all cases. For V and Fe, an obvious peak shift was observed, which demonstrated that V and Fe were also oxidized to V^V[34] and Fe^{III}[35−37] (Figure 3i−v). The electron successfully transferred from O_2 to the materials to form oxidized ε-Keggin molybdates. The reduction tends to form molecular ε-Keggin polyoxomolybdates. Most of the ε-Keggin molybdates are reduced compounds, and as far as we know, no result shows the fully oxidized Mo in ε-Keggin molybdates.[25,38] The formation of the 3D framework probably increased the redox stability.

TPO−MS confirmed that the oxidation of $\mathbf{MoFe_{0.22}O}$ and $\mathbf{MoFeV_{\mathit{x}}O}$ was caused by reaction with O_2. TPO−MS profiles showed that $\mathbf{MoFe_{0.22}O}$ and $\mathbf{MoFeV_{\mathit{x}}O}$ started to react with O_2 below 100 °C (Figure 4a−f); the materials kept reacting with O_2 up to 400 °C. Compared with the other material based on ε-Keggin POM, **MoZnO**, the temperature for the reaction with O_2 was obviously higher (200 °C) than those of $\mathbf{MoFe_{0.22}O}$ and $\mathbf{MoFeV_{\mathit{x}}O}$, which demonstrated the superiority of Fe-based materials in reacting with O_2 at a low temperature.

Oxidation of $\mathbf{MoFe_{0.22}O}$ occurred even at room temperature (25 °C), suggesting a unique O_2 adsorption−desorption isotherm. The material was calcined at 200 °C for 2 h under high vacuum to remove the occupied water and NH_3 in the material before O_2 adsorption. The adsorption−desorption isotherms of O_2 at 25 °C are shown in Figure 4g,j. The O_2

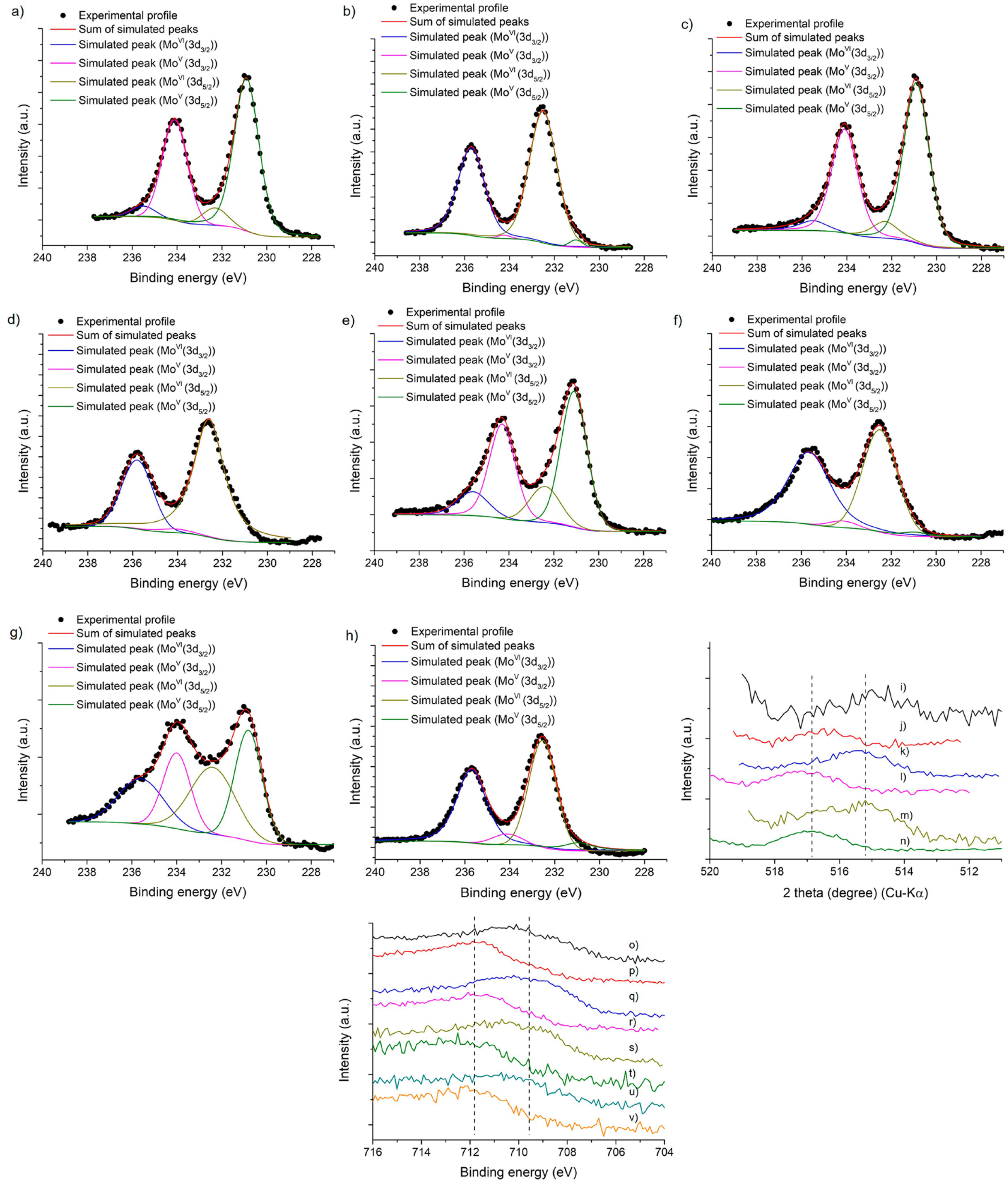

Figure 3. XPS profiles of (a) Mo in $\mathbf{MoFe_{0.22}O}$, (b) Mo in $\mathbf{MoFe_{0.22}OAC150}$, (c) Mo in $\mathbf{MoFe_{0.17}V_{0.07}O}$, (d) Mo in $\mathbf{MoFe_{0.17}V_{0.07}OAC150}$, (e) Mo in $\mathbf{MoFe_{0.14}V_{0.12}O}$, (f) Mo in $\mathbf{MoFe_{0.14}V_{0.12}OAC150}$, (g) Mo in $\mathbf{MoFe_{0.11}V_{0.18}O}$, and (h) Mo in $\mathbf{MoFe_{0.11}V_{0.18}OAC150}$; V in the materials (i) $\mathbf{MoFe_{0.17}V_{0.07}O}$, (j) $\mathbf{MoFe_{0.17}V_{0.07}OAC150}$, (k) $\mathbf{MoFe_{0.14}V_{0.12}O}$, (l) $\mathbf{MoFe_{0.14}V_{0.12}OAC150}$, (m) $\mathbf{MoFe_{0.11}V_{0.18}O}$, and (n) $\mathbf{MoFe_{0.11}V_{0.18}OAC150}$; and Fe in the materials (o) $\mathbf{MoFe_{0.22}O}$, (p) $\mathbf{MoFe_{0.22}OAC150}$, (q) $\mathbf{MoFe_{0.17}V_{0.07}O}$, (r) $\mathbf{MoFe_{0.17}V_{0.07}OAC150}$, (s) $\mathbf{MoFe_{0.14}V_{0.12}O}$, (t) $\mathbf{MoFe_{0.14}V_{0.12}OAC150}$, (u) $\mathbf{MoFe_{0.11}V_{0.18}O}$, and (v) $\mathbf{MoFe_{0.11}V_{0.18}OAC150}$.

uptake remarkably increased under the low-pressure condition, corresponding to O_2 adsorbing in the micropores of the materials. Adsorption of O_2 in the material was, however, irreversible, and an obvious hysteresis of adsorption−desorption isotherms was observed. Most of the O_2 adsorbed in the material was not able to desorb from the material even if

DOI: 10.1021/acs.inorgchem.9b00502
Inorg. Chem. XXXX, XXX, XXX−XXX

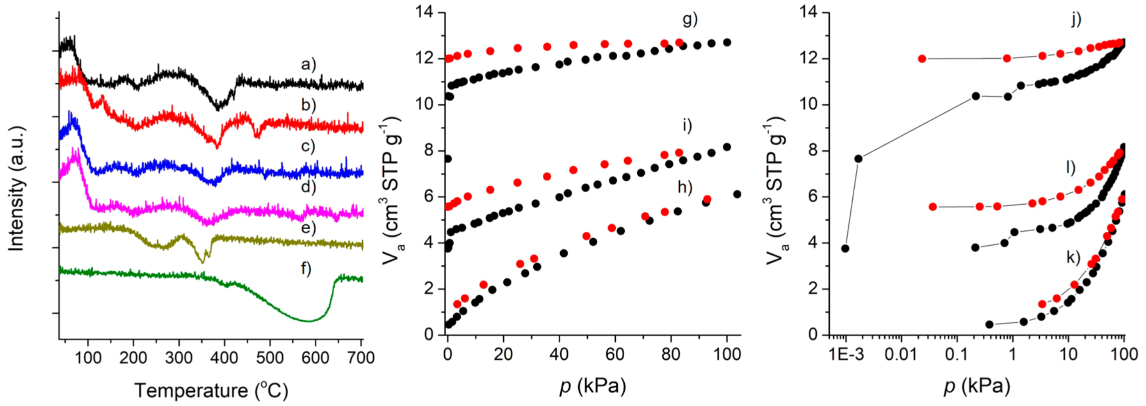

Figure 4. TPO profiles of (a) **$MoFe_{0.22}O$**, (b) **$MoFe_{0.17}V_{0.07}O$**, (c) **$MoFe_{0.14}V_{0.12}O$**, (d) **$MoFe_{0.11}V_{0.18}O$**, (e) **MoZnO**, and (f) MoO_2. O_2 adsorption−desorption isotherms of (g) **$MoFe_{0.22}O$**, (h) **MoZnO**, and (i) **FeMoZnO** at 25 °C. O_2 adsorption−desorption isotherms at low pressure of (j) **$MoFe_{0.22}O$**, (k) **MoZnO**, and (l) **FeMoZnO** at 25 °C: adsorption branch (black), desorption branch (red).

at low pressure. Mo^V was partially oxidized to Mo^{VI} after O_2 adsorption at room temperature (Figure S12a,b), and Fe in the material was also oxidized (Figure S12c,d). We assumed that the adsorbed O_2 reacted with Mo^V to form Mo^{VI} and H_2O, which blocked the micropore and inhibited the further oxidation.

Fe was critical for the oxidation of **$MoFe_{0.22}O$** with O_2 at room temperature. The isostructural material of **$MoFe_{0.22}O$**, **MoZnO**, did not show the same O_2 adsorption−desorption isotherm (Figure 4h,k). The isotherm of **MoZnO** was reversible, and the O_2 adsorbed amount was low. Furthermore, the Fe exchange was further carried out for **MoZnO**, and the resulting material was denoted as **FeMoZnO**. After the ion-exchange process, XRD patterns and FTIR spectra did not change (Figure S13), demonstrating that the basic structure of **MoZnO** remained the same. Elemental analysis demonstrated that a certain amount of Fe was successfully introduced (see the Experimental Section for elemental analysis). **FeMoZnO** became active for the oxidation at room temperature, which indicated that the Fe cation was responsible for this phenomenon (Figure 4i,l). Thus, we assumed that O_2 could be activated in the material at a low temperature probably in the Fe site, which immediately oxidized Mo and Fe in the material.

Structure Change. The structure change of **$MoFe_{0.22}O$** during oxidation at 150 °C was investigated in detail. The diffraction peak shifted to a higher angle, indicating that lattice parameters of the materials decreased after calcination (Figure 1i−p and Figure S11). The structures of the materials were analyzed by the Rietveld refinement (Figure S4b). Although the crystal structure of the material was almost the same, the location of Mo in **$MoFe_{0.22}O$** changed after calcination in air (Figure 5). ε-Keggin was formed by 4 Mo_3O_{13} trimers (Figure 5b), which were arranged in a tetrahedral manner by connecting with Mo_2O_{10} dimers (Figure 5c). In the as-synthesized **$MoFe_{0.22}O$**, the distance of Mo···Mo in the Mo_3O_{13} trimer was 3.410 Å. After calcination in air, the distance decreased dramatically to 3.260 Å (Figure 5). The distance of Mo···Mo in the Mo_2O_{10} dimer increased from 2.646 to 2.910 Å. The Mo···Mo distance change would probably cause the Mo−O bonding state change.

The materials after calcination at different temperatures were also studied by FTIR (Figure 1a−h and Figure S14). FTIR spectra of the materials drastically changed after calcination at 150 °C, and new IR bands at 796, 696, and 635 cm^{-1} were generated; the original IR band at 753 cm^{-1} disappeared. This indicates that the bonding state and the local structure changed after calcination at 150 °C. The Mo···Mo distance change probably caused the Mo−O−Mo bond length change, resulting in the FTIR signal change, which was in good agreement with the XRD analysis.

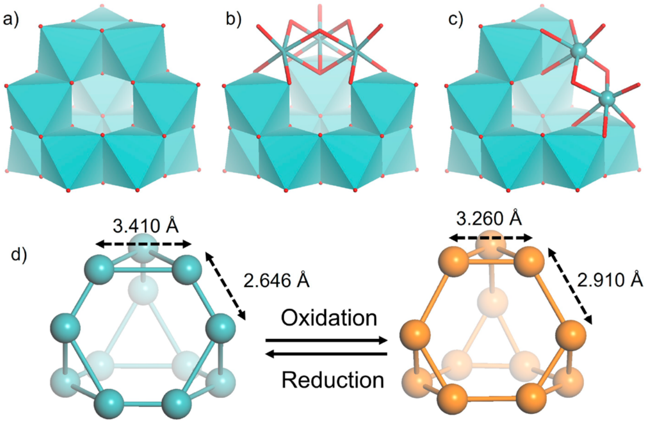

Figure 5. Structural representations of the ε-Keggin unit: (a) polyhedral representation, ball-and-stick representation of (b) the Mo_3O_{13} trimer and (c) the Mo_2O_{10} dimer in the ε-Keggin unit, and (d) ball representation of the material during redox; Mo (blue), Mo oxidized (orange), O (red).

In the case of the oxidation of **$MoFe_{0.22}O$** at room temperature, the XRD patterns of **$MoFe_{0.22}O$** before and after O_2 adsorption showed the diffraction peak shift, the diffraction peak intensity change, and newly generated FTIR bands (Figure S13l), which were in good agreement with the material after calcination at 150 °C in air, indicating the molecular structure change.

Reduction. The electron-transfer process for **$MoFe_{0.22}O$** was reversible. **$MoFe_{0.22}OAC150$** was further reduced by H_2 at 150, 200, 250, and 300 °C; the resulting materials were denoted as **$MoFe_{0.22}OAC150HC150$**, **$MoFe_{0.22}OAC150HC200$**, **$MoFe_{0.22}OAC150HC250$**, and **$MoFe_{0.22}OAC150HC300$**. XRD demonstrated that the material was stable when the treatment temperature was below 250 °C (Figure S15a−f). After reduction, the IR bands of **$MoFe_{0.22}O$** started to generate when the treatment temperature was 150 °C (Figure S15i), which indicated that **$MoFe_{0.22}OAC150$** was able to be reduced using H_2 as a reductant. With an increase of

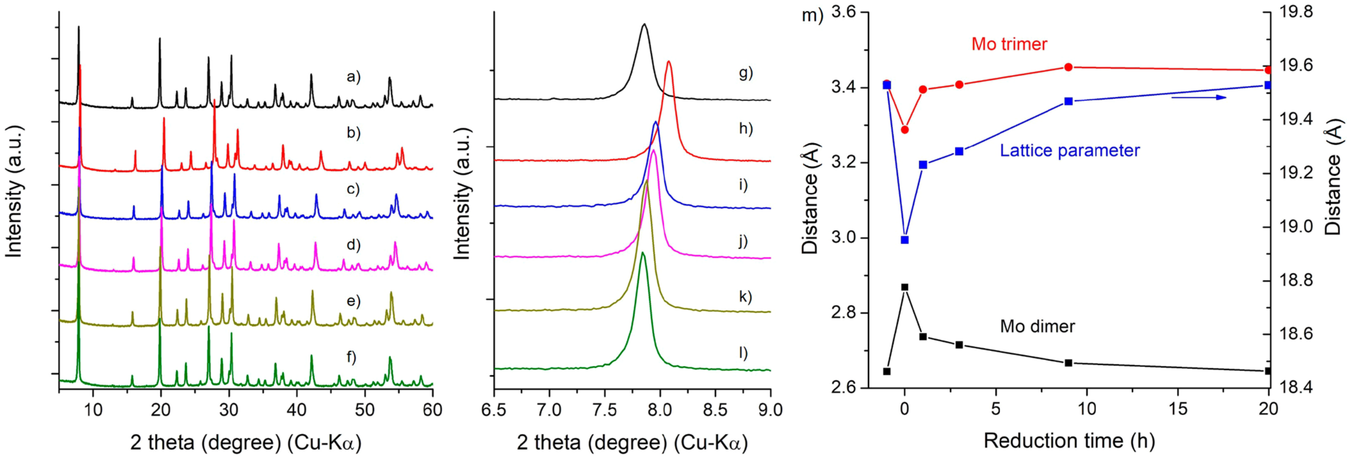

Figure 6. XRD patterns of (a) **MoFe$_{0.22}$O**; (b) **MoFe$_{0.22}$OAC150**; **MoFe$_{0.22}$OAC150** reduced by $N_2H_6SO_4$ for (c) 1 h, (d) 3 h, (e) 9 h, and (f) 20 h. Enlarged XRD patterns of (g) **MoFe$_{0.22}$O**; (h) **MoFe$_{0.22}$OAC150**; **MoFe$_{0.22}$OAC150** reduced by $N_2H_6SO_4$ for (i) 1 h, (j) 3 h, (k) 9 h, and (l) 20 h. (m) Lattice parameters and Mo···Mo distance change during the treatments.

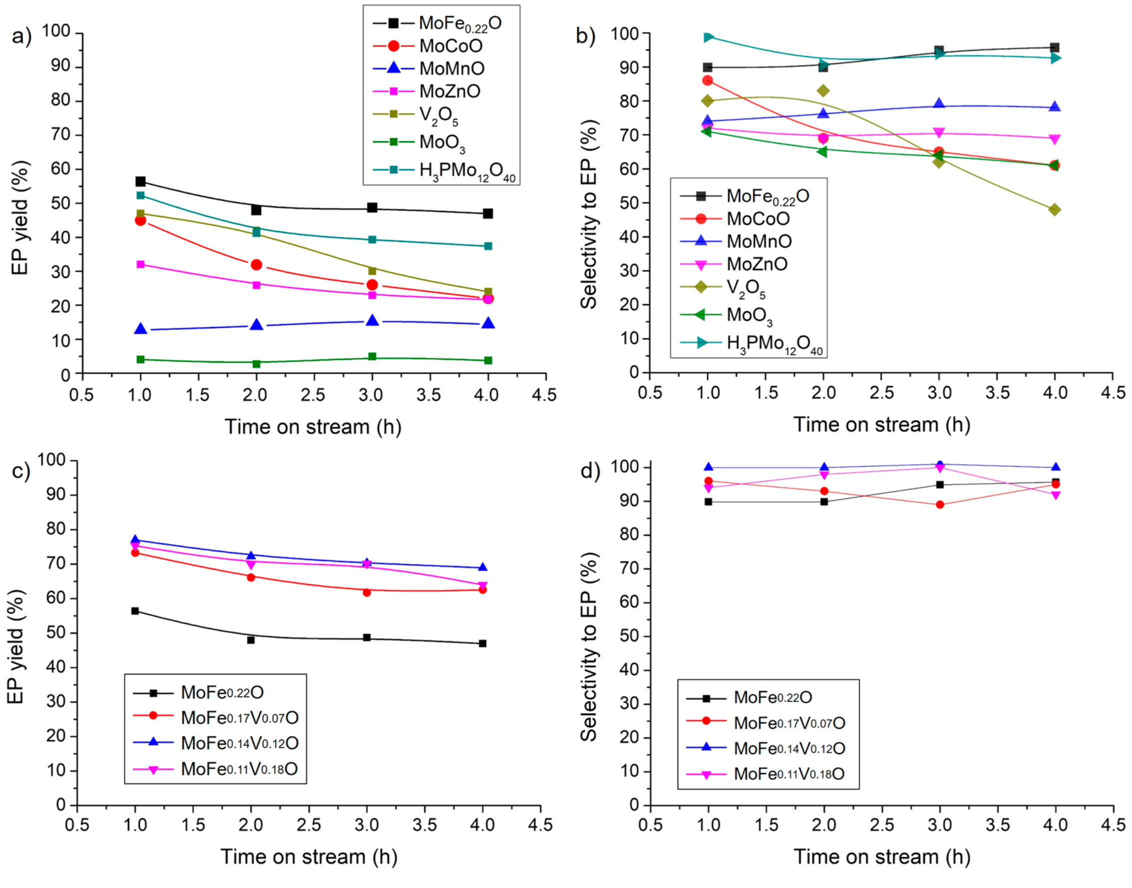

Figure 7. Catalytic activity of the materials for EL oxidation to form EP. (a) EP yield and (b) selectivity to EP of different catalysts. (c) EP yield and (d) selectivity to EP of the materials based on different V contents. Reaction conditions: air 20 mL/min (N_2 15.6 mL/min, O_2 4.2 mL/min), EL 1.95 mL/min, catalyst 0.5 g, and temperature 200 °C.

the reduction temperature to 200 °C, most of the IR signals observed on **MoFe$_{0.22}$O** regenerated (Figure S15j,k), which indicated that **MoFe$_{0.22}$OAC150** was reduced by H_2, and the bonding state change was reversible.

Furthermore, **MoFe$_{0.22}$OAC150** was also able to be reduced by $N_2H_6SO_4$ in aqueous solution at room temperature with the basic crystal structure maintained (Figure 6a–l). The XRD patterns of the materials were analyzed by the Rietveld refinement (Figure S4c–f). The result indicated that, as the reaction time prolonged, the lattice parameter of the material increased (Figure 6m). The distance of Mo···Mo in the Mo_3O_{13} trimer increased from 3.260 to 3.441 Å. The distance of the Mo_2O_{10} dimer decreased. The result indicated that the Mo···Mo distance change was reversible.

The redox cycle of the material was completed using O_2 and reducing agents with the basic crystal structures of the materials maintained, which strongly indicated that

$MoFe_{0.22}O$-based materials were able to be used as catalysts for selective oxidation based on an electron-transfer process.

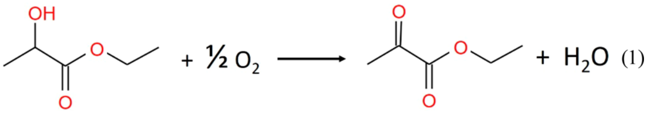

EL Oxidation. Pyruvates have industrial applications as important raw compounds for the production of food additives, perfumes, and electronic materials.[39−41] Currently, pyruvates are still produced via an energy-consuming process by high-temperature decomposition of tartaric acid with stoichiometric $KHSO_4$ as a dehydrating agent.[42] Obtaining pyruvates from biomass-derived compounds, such as lactates, is an ideal approach because lignocellulosic biomass is a renewable carbon source, which is important for a sustainable society. Several effective catalytic systems have been developed for pyruvates production via oxidation of lactates.[42−46] Electron-transfer-based O_2 activation is important for oxidative dehydrogenation of hydroxyl through the redox process, and **$MoFeV_xO$** will be able to be used as catalysts for EL oxidation to form EP.

Different zeolitic transition metal oxides based on ε-Keggin POM units were used as catalysts for the oxidation of EL to EP at 200 °C using O_2 as an oxidant (eq 1). The EP yield and the selectivity to EP are shown in Figure 7a,b. **$MoFe_{0.22}O$** showed the best performance among the ε-Keggin POM-based zeolitic transition metal oxides. The EP yield and the selectivity to EP of **$MoFe_{0.22}O$** were higher than those of other ε-Keggin POM-based catalysts. As the reaction time prolonged, the catalytic activity slightly decayed while the selectivity to EP kept constant.

The single metal oxides, such as MoO_3 and V_2O_5, were not active (Figure 7a,b). V_2O_5 was more active than MoO_3, but the catalytic activity and the selectivity to EP declined obviously. This indicated that the complexity of the material was important for catalysis. The reaction was also carried out using other materials as catalysts. Compared with the heteropoly acid, $H_3PMo_{12}O_{40}$, the activity of the material at 200 °C was also higher. After incorporating Fe in **MoZnO**, the activity of the material increased, indicating that Fe was critical for the reaction (Figure S16). Compared with the reported catalysts, our material also showed high activity (Table S9).

V-oxide-based materials were redox-active,[47,48] which enhances the redox ability of the materials.[49] Incorporating V in **$MoFe_{0.22}O$** increased the catalytic activity of the material without change of the selectivity (Figure 7c). The EP yield increased from ca. 50% (**$MoFe_{0.22}O$**) to ca. 65% (**$MoFeV_xO$**) while the selectivity to EP was almost constant (Figure 7d). However, the content of V seems not to be critical to further increase the activity. With different V contents, the yield of EP did not change remarkably. The reasons might be that increasing the V content did not remarkably increase the isolated V species in the material, because the V species in **$MoFe_{0.14}V_{0.12}O$** and **$MoFe_{0.11}V_{0.18}O$** was over 1 per Keggin unit, which might be the real active site for selective oxidation.[50,51]

The EP yield increased with the increase of the reaction temperature over **$MoFe_{0.14}V_{0.12}O$** as a model catalyst (Figure S17a,b). When the temperature was 150 °C, the yield was low (ca. 25%). As the temperature increased, the yield increased accordingly. The selectivity to EP was over 90%. When the reaction was carried out at 185−200 °C, the selectivity to EP was the highest. Therefore, the suitable reaction temperature was 200 °C because both the EP yield and selectivity were high. The effect of the flow rate of EL was investigated. The yield of EP was increased by decreasing the flow rate of EL without change of the selectivity to EP (Figure S17c,d). The flow rate of air also affected the activity of the material. The activity increased with the decrease of the air flow. The effect of the catalyst amount was investigated. When the catalyst amount decreased, the yield of EP decreased dramatically. The selectivity to EP did not change remarkably (Figure S17e,f).

After the reaction, **$MoFe_{0.22}O$** and **$MoFeV_xO$** were characterized by XRD. The same patterns were observed before and after the reaction, indicating that the materials were stable during the reaction (Figure S18).

The reaction was carried out by a stepwise method using **$MoFe_{0.22}O$** as a model catalyst (Figures S19 and S20). The material was first calcined in air (20 mL/min) at 200 °C for 20 min, and the resulting material was denoted as **$MoFe_{0.22}OAC$**; then, air was stopped, and N_2 was flowed (20 mL/min) for 20 min. After that, EL was introduced (1.95 mL/min) with flowing N_2, and the reaction was monitored by gas chromatography with flame-ionization detection (GC-FID). As shown in Figure S19a−d, **$MoFe_{0.22}OAC$** oxidized EL to form EP as a product with the reduction of **$MoFe_{0.22}OAC$**. The peak of EP declined as the reaction time prolonged. After reacting for 80 min, almost no EP was detected, indicating that the material was completely reduced, and the resulting material was denoted as **$MoFe_{0.22}OEL$**. **$MoFe_{0.22}OAC$** after the reaction with EL could be regenerated by reacting with O_2 once again. After regeneration, the activity of the material recovered (Figure S19e−h). **$MoFe_{0.22}OEL$** at 200 °C was characterized by FTIR (Figure S21a−c), which indicated that the peaks for **$MoFe_{0.22}O$** were generated, and the peaks for the **$MoFe_{0.22}OAC$** disappeared completely, which demonstrated that **$MoFe_{0.22}OAC$** could be reduced by EL to form **$MoFe_{0.22}OEL$**. XRD patterns of **$MoFe_{0.22}O$** did not change, demonstrating that the material was stable (Figure S21d−f).

On the basis of the above experiments, the reaction mechanism was proposed. The reaction probably took place under an electron-transfer pathway (Figure S20). **$MoFe_{0.22}O$** was oxidized with O_2 to form **$MoFe_{0.22}OAC$**, which further reacted with EL to form EP; meanwhile, **$MoFe_{0.22}OAC$** was reduced simultaneously. **$MoFe_{0.22}OEL$** was reoxidized with O_2, and a new catalytic cycle started. The easy redox ability of **$MoFe_{0.22}O$** enabled the material to be oxidized easily.

■ CONCLUSION

In summary, zeolitic iron molybdate and iron vanadomolybdates were composed of ε-Keggin POM units that were linked by Fe ions. V substituted the POM units and linkers of the material, and the content of V could be controlled. The materials activated O_2 via an electron-transfer process leading to the oxidation of the materials easily even at room temperature. The oxidized material could be reduced using reductants reversibly. The basic crystal structures were stable while the bonding states of the materials changed during the redox reactions. The materials showed catalytic activity for the selective oxidation of EL to EP using O_2 as an oxidant.

■ ASSOCIATED CONTENT

Ⓢ Supporting Information

The Supporting Information is available free of charge on the ACS Publications website at DOI: 10.1021/acs.inorgchem.9b00502.

> Additional XRD patterns, FTIR spectra, XPS profiles, SEM images, EDX-mapping images, Rietveld refinements, a TEM image, TPD−MS profiles, N_2 adsorption−desorption isotherms, CO_2 adsorption isotherms, catalytic results, a stepwise reaction scheme, the atomic position of the materials, crystallographic information of the materials, and catalytic activity of the reported catalysts (PDF)

■ AUTHOR INFORMATION

Corresponding Authors

*E-mail: zhangzhenxin@nbu.edu.cn.
*E-mail: uedaw@kanagawa-u.ac.jp.

ORCID

Zhenxin Zhang: 0000-0002-9609-4691
Satoshi Ishikawa: 0000-0003-4372-4108
Toru Murayama: 0000-0001-5105-3290
Masahiro Sadakane: 0000-0001-7308-563X

Notes

The authors declare no competing financial interest.

■ ACKNOWLEDGMENTS

This work was financially supported by the National Natural Science Foundation of China (Grant 21801141).

■ REFERENCES

(1) Prech, J.; Pizarro, P.; Serrano, D. P.; Cejika, J. From 3D to 2D Zeolite Catalytic Materials. *Chem. Soc. Rev.* **2018**, *47*, 8263−8306.

(2) Borfecchia, E.; Beato, P.; Svelle, S.; Olsbye, U.; Lamberti, C.; Bordiga, S. Cu-CHA−a Model System for Applied Selective Redox Catalysis. *Chem. Soc. Rev.* **2018**, *47*, 8097−8133.

(3) Dusselier, M.; Davis, M. E. Small-Pore Zeolites: Synthesis and Catalysis. *Chem. Rev.* **2018**, *118*, 5265−5329.

(4) Hwang, J.; Rao, R. R.; Giordano, L.; Katayama, Y.; Yu, Y.; Shao-horn, Y. Perovskites in Catalysis and Electrocatalysis. *Science* **2017**, *358*, 751−756.

(5) Kuznetsov, D. A.; Han, B.; Yu, Y.; Rao, R. R.; Hwang, J. Tuning Redox Transitions via Inductive Effect in Metal Oxides and Complexes, and Implications in Oxygen Electrocatalysis. *Joule* **2018**, *2*, 1−20.

(6) Luo, W.; Wang, J.; Hu, J.; Ji, Y.; Streb, C.; Song, Y. Composite Metal Oxide-Carbon Nanotube Electrocatalysts for the Oxygen Evolution and Oxygen Reduction Reactions. *ChemElectroChem* **2018**, *5*, 2850−2856.

(7) Zhang, Z.; Zhu, Q.; Sadakane, M.; Murayama, T.; Hiyoshi, N.; Yamamoto, A.; Hata, S.; Yoshida, H.; Ishikawa, S.; Hara, M.; Ueda, W. A Zeolitic Vanadotungstate Family with Structural Diversity and Ultrahigh Porosity for Catalysis. *Nat. Commun.* **2018**, *9*, 3789.

(8) Sadakane, M.; Kodato, K.; Kuranishi, T.; Nodasaka, Y.; Sugawara, K.; Sakaguchi, N.; Nagai, T.; Matsui, Y.; Ueda, W. Molybdenum-Vanadium-Based Molecular Sieves with Microchannels of Seven-Membered Rings of Corner-Sharing Metal Oxide Octahedra. *Angew. Chem., Int. Ed.* **2008**, *47*, 2493−2496.

(9) Sadakane, M.; Watanabe, N.; Katou, T.; Nodasaka, Y.; Ueda, W. Crystalline Mo_3VO_x Mixed-Metal-Oxide Catalyst with Trigonal Symmetry. *Angew. Chem., Int. Ed.* **2007**, *46*, 1493−1496.

(10) Sadakane, M.; Yamagata, K.; Kodato, K.; Endo, K.; Toriumi, K.; Ozawa, Y.; Ozeki, T.; Nagai, T.; Matsui, Y.; Sakaguchi, N.; Pyrz, W. D.; Buttrey, D. J.; Blom, D. A.; Vogt, T.; Ueda, W. Synthesis of Orthorhombic Mo-V-Sb Oxide Species by Assembly of Pentagonal Mo_6O_{21} Polyoxometalate Building Blocks. *Angew. Chem., Int. Ed.* **2009**, *48*, 3782−3786.

(11) Zhan, C.; Cameron, J. M.; Gabb, D.; Boyd, T.; Winter, R. S.; Vila, L.; Mitchell, S. G.; Glatzel, S.; Breternitz, J.; Gregory, D. H.; Long, D.; Macdonell, A.; Cronin, L. A Metamorphic Inorganic Framework That Can Be Switched between Eight Single-Crystalline States. *Nat. Commun.* **2017**, *8*, 14185.

(12) Mitchell, S. G.; Streb, C.; Miras, H. N.; Boyd, T.; Long, D.-L.; Cronin, L. Face-Directed Self-Assembly of an Electronically Active Archimedean Polyoxometalate Architecture. *Nat. Chem.* **2010**, *2*, 308−312.

(13) Zhang, Z.; Sadakane, M.; Murayama, T.; Izumi, S.; Yasuda, N.; Sakaguchi, N.; Ueda, W. Tetrahedral Connection of ε-Keggin-Type Polyoxometalates to Form an All-Inorganic Octahedral Molecular Sieve with an Intrinsic 3D Pore System. *Inorg. Chem.* **2014**, *53* (2), 903−911.

(14) Zhang, Z.; Sadakane, M.; Murayama, T.; Sakaguchi, N.; Ueda, W. Preparation, Structural Characterization, and Ion-Exchange Properties of Two New Zeolite-like 3D Frameworks Constructed by ε-Keggin-Type Polyoxometalates with Binding Metal Ions, $H_{11.4}[ZnMo_{12}O_{40}Zn_2]^{1.5-}$ and $H_{7.5}[Mn_{0.2}Mo_{12}O_{40}Mn_2]^{2.1-}$. *Inorg. Chem.* **2014**, *53*, 7309−7318.

(15) Zhang, Z.; Sadakane, M.; Noro, S.; Murayama, T.; Kamachi, T.; Yoshizawa, K.; Ueda, W. Selective Carbon Dioxide Adsorption of ε-Keggin- Type Zincomolybdate-Based Purely Inorganic 3D Frameworks. *J. Mater. Chem. A* **2015**, *3*, 746−755.

(16) Zhang, Z.; Ishikawa, S.; Tsuboi, Y.; Sadakane, M.; Murayama, T.; Ueda, W. New Crystalline Complex Metal Oxides Created by Unit- Synthesis and Their Catalysis Based on Porous and Redox Properties. *Faraday Discuss.* **2016**, *188*, 81−98.

(17) Neumann, R. Activation of Molecular Oxygen, Polyoxometalates, and Liquid-Phase Catalytic Oxidation. *Inorg. Chem.* **2010**, *49*, 3594−3601.

(18) Kim, M.; Chamack, M.; Geletii, Y. V.; Hill, C. L. Synergetic Catalysis of Copper and Iron in Oxidation of Reduced Keggin Heteropolytungstates by Dioxygen. *Inorg. Chem.* **2018**, *57*, 311−318.

(19) Kim, M.; Weinstock, I. A.; Geletii, Y. V.; Hill, C. L. Oxidation of Reduced Keggin Heteropolytungstates by Dioxygen in Water Catalyzed by Cu(II). *ACS Catal.* **2015**, *5*, 7048−7054.

(20) Igarashi, T.; Zhang, Z.; Haioka, T.; Iseki, N.; Hiyoshi, N.; Sakaguchi, N.; Kato, C.; Nishihara, S.; Inoue, K.; Yamamoto, A.; Yoshida, H.; Tsunoji, N.; Ueda, W.; Sano, T.; Sadakane, M. Synthesis of ε-Keggin-Type Cobaltomolybdate-Based 3D Framework Material and Characterization Using Atomic-Scale HAADF-STEM and XANES. *Inorg. Chem.* **2017**, *56*, 2042−2049.

(21) Boultif, A.; Louer, D. Powder Pattern Indexing with the Dichotomy Method. *J. Appl. Crystallogr.* **2004**, *37*, 724−731.

(22) Neumann, M. A. X-Cell: A Novel Indexing Algorithm for Routine Tasks and Difficult Cases. *J. Appl. Crystallogr.* **2003**, *36*, 356−365.

(23) Palatinus, L.; Chapuis, G. SUPERFLIP - a Computer Program for the Solution of Crystal Structures by Charge Flipping in Arbitrary Dimensions. *J. Appl. Crystallogr.* **2007**, *40*, 786−790.

(24) Young, R. A. *The Rietveld Method*; Young, R. A., Ed.; Oxford University Press: Oxford, 1995.

(25) Müller, A.; Beugholt, C.; Kögerler, P.; Bögge, H.; Bud’ko, S.; Luban, M. $[Mo^{V}_{12}O_{30}(\mu 2\text{-}OH)_{10}H_2\{Ni^{II}(H_2O)_3\}_4]$, a Highly Symmetrical ε-Keggin Unit Capped with Four NiII Centers: Synthesis and Magnetism. *Inorg. Chem.* **2000**, 39 (23), 5176−5177.

(26) Zhang, Z.; Sadakane, M.; Murayama, T.; Ueda, W. Investigation of the Formation Process of Zeolite-like 3D Frameworks Constructed with ε-Keggin-Type Polyoxovanadomolybdates with Binding Bismuth Ions and Preparation of a Nano-Crystal. *Dalt. Trans.* **2014**, *43*, 13584−13590.

(27) Bond, G. C.; Flamerz, S. Structure and Reactivity of Titania-Supported Oxides: IV. Characterisation of Dried Vanadia/Titania Catalyst Precursors. *Appl. Catal.* **1989**, *46*, 89−102.

(28) Horvath, B.; Strutz, J.; Geyer-Lippmann, J.; Horvath, E. G. Preparation, Properties, and ESCA Characterization of Vanadium Surface Compounds on Silicagel. III. *Z. Anorg. Allg. Chem.* **1981**, *483*, 181−192.

(29) Linnenberg, O.; Moors, M.; Sole, A.; Lo, X.; Ba, C.; Kentzinger, E.; Pyckhout-Hintzen, W.; Monakhov, K. Y. Molecular Characteristics of a Mixed-Valence Polyoxovanadate $\{V^{IV/V}{}_{18}O_{42}\}$ in Solution and at the Liquid−Surface Interface. *J. Phys. Chem. C* **2017**, *121*, 10419−10429.

(30) McIntyre, N. S.; Zetaruk, D. G. X-Ray Photoelectron Spectroscopic Studies of Iron Oxides. *Anal. Chem.* **1977**, *49*, 1521−1529.

(31) Carver, J. C.; Schweitzer, G. K.; Carlson, T. A. Use of X-Ray Photoelectron Spectroscopy to Study Bonding in Cr, Mn, Fe, and Co Compounds. *J. Chem. Phys.* **1972**, *57*, 973−982.

(32) Hawn, D. D.; DeKoven, B. M. Deconvolution as a Correction for Photoelectron Inelastic Energy Losses in the Core Level XPS Spectra of Iron Oxides. *Surf. Interface Anal.* **1987**, *10*, 63−74.

(33) Anwar, M.; Hogarth, C. A.; Bulpett, R. Effect of Substrate Temperature and Film Thickness on the Surface Structure of Some Thin Amorphous Films of MoO3 Studied by X-Ray Photoelectron Spectroscopy (ESCA). *J. Mater. Sci.* **1989**, *24*, 3087−3090.

(34) Lindblad, T.; Rebenstorf, B.; Yan, Z.-G.; Andersson, S. L. T. Characterization of Vanadia Supported on Amorphous $AlPO_4$ and Its Properties for Oxidative Dehydrogenation of Propane. *Appl. Catal., A* **1994**, *112*, 187−208.

(35) Kim, Y. I.; Hatfield, W. E. Electrical, Magnetic and Spectroscopic Properties of Tetrathiafulvalene Charge Transfer Compounds with Iron, Ruthenium, Rhodium and Iridium Halides. *Inorg. Chim. Acta* **1991**, *188*, 15−24.

(36) Langevoort, J. C.; Sutherland, I.; Hanekamp, L. J.; Gellings, P. J. On the Oxide Formation on Stainless Steels AISI 304 and Incoloy 800H Investigated with XPS. *Appl. Surf. Sci.* **1987**, *28*, 167−179.

(37) Allen, G. C.; Curtis, M. T.; Hooper, A. J.; Tucker, P. M. X-Ray Photoelectron Spectroscopy of Iron−oxygen Systems. *J. Chem. Soc., Dalton Trans.* **1974**, 1525−1530.

(38) Mialane, P.; Dolbecq, A.; Lisnard, L.; Mallard, A. Amenable to Scale-up, Geared to Provide Access to Analogues, and Involves Only One Protecting-Group Manipulation. *Angew. Chem.* **2002**, *114*, 2504−2507.

(39) Maki-Arvela, P.; Simakova, I. L.; Salmi, T.; Murzin, D. Y. Production of Lactic Acid/Lactates from Biomass and Their Catalytic Transformations to Commodities. *Chem. Rev.* **2014**, *114*, 1909−1971.

(40) Corma, A.; Iborra, S.; Velty, A. Chemical Routes for the Transformation of Biomass into Chemicals. *Chem. Rev.* **2007**, *107*, 2411−2502.

(41) Yasukawa, T.; Ninomiya, W.; Ooyachi, K.; Aoki, N.; Mae, K. Enhanced Production of Ethyl Pyruvate Using Gas−liquid Slug Flow in Microchannel. *Chem. Eng. J.* **2011**, *167*, 527−530.

(42) Zhang, W.; Ensing, B.; Rothenberg, G.; Shiju, N. R. Designing Effective Solid Catalysts for Biomass Conversion: Aerobic Oxidation of Ethyl Lactate to Ethyl Pyruvate. *Green Chem.* **2018**, *20*, 1866−1873.

(43) Zhang, W.; Innocenti, G.; Oulego, P.; Gitis, V.; Wu, H.; Ensing, B.; Cavani, F.; Rothenberg, G.; Shiju, N. R. Highly Selective Oxidation of Ethyl Lactate to Ethyl Pyruvate Catalyzed by Mesoporous Vanadia − Titania. *ACS Catal.* **2018**, *8*, 2365−2374.

(44) Zhao, X.; Zhang, C.; Xu, C.; Li, H.; Huang, H.; Song, L.; Li, X. Kinetics Study for the Oxidative Dehydrogenation of Ethyl Lactate to Ethyl Pyruvate over $MoVNbO_x$ Based Catalysts. *Chem. Eng. J.* **2016**, *296*, 217−224.

(45) Hayashi, H.; Sugiyama, S.; Kokawa, N.; Koto, K. Additive Telluromolybdates as Catalyst for Vapor-Phase Selective Oxidation of Ethyl Lactate to Pyruvate. *Appl. Surf. Sci.* **1997**, *122*, 378−381.

(46) Ramos-fernandez, E. V.; Geels, N. J.; Shiju, N. R.; Rothenberg, G. Titania-Catalysed Oxidative Dehydrogenation of Ethyl Lactate: Effective yet Selective Free-Radical Oxidation. *Green Chem.* **2014**, *16*, 3358−3363.

(47) Linnenberg, O.; Mayerl, L.; Monakhov, K. Y. The Heck Reaction as a Tool to Expand Polyoxovanadates towards Thiol-Sensitive Organic−inorganic Hybrid Fluorescent Switches. *Dalt. Trans.* **2018**, *47*, 14402−14407.

(48) Stuckart, M.; Monakhov, K. Y. Vanadium: Polyoxometalate Chemistry. In *Encyclopedia of Inorganic and Bioinorganic Chemistry*; John Wiley & Sons, 2018.

(49) Zhao, H.; Bennici, S.; Shen, J.; Auroux, A. Nature of Surface Sites of $V_2O_5-TiO_2/SO_4^{2-}$ Catalysts and Reactivity in Selective Oxidation of Methanol to Dimethoxymethane. *J. Catal.* **2010**, *272*, 176−189.

(50) Bulánek, R.; Čičmanec, P.; Sheng-Yang, H.; Knotek, P.; Čapek, L.; Setnička, M. Effect of Preparation Method on Nature and Distribution of Vanadium Species in Vanadium-Based Hexagonal Mesoporous Silica Catalysts: Impact on Catalytic Behavior in Propane ODH. *Appl. Catal., A* **2012**, *415−416*, 29−39.

(51) Piumetti, M.; Bonelli, B.; Massiani, P.; Dzwigaj, S.; Rossetti, I.; Casale, S.; Armandi, M.; Thomas, C.; Garrone, E. Effect of Vanadium Dispersion and of Support Properties on the Catalytic Activity of V-Containing Silicas. *Catal. Today* **2012**, *179*, 140−148.